Variational Quantum Linear Solver via Block Encoding for the Poisson Equation

Viraj Dsouza,[1,*] Ayush Singhal,[1,2,†] Alex Khan,[1,‡] Rut Lineswala,[1] and Abhishek Chopra[1]

[1]*BosonQ Psi Corp., Syracuse, New York 13202, USA*

[2]*Department of Computer Science, University of Maryland, College Park, Maryland 20742, USA*

We present a variational quantum linear solver (VQLS) for the Poisson equation built on an exact block encoding of the discrete Laplacian, and demonstrate its performance on physically motivated benchmarks. Unlike LCU-based VQLS where the number of distinct circuits required per cost-function evaluation is $\mathcal{O}(L^2)$, where L is the number of terms in the LCU decomposition of the discrete Laplacian operator, this approach requires only a single circuit for cost evaluation. We further empirically demonstrate that the choice of classical optimizer materially affects where the variational optimization ceases to make progress. The solver is benchmarked on three problems: a Poisson equation with sinusoidal forcing and a steady-state heat conduction problem with a localized Gaussian source, both with Dirichlet boundaries, and the pressure-Poisson equation of a two-dimensional lid-driven cavity flow, in which the solver is invoked once per time step under Neumann boundary conditions.

arXiv:2608.19655v1 [quant-ph] 20 Aug 2026

I. INTRODUCTION

Solving large linear systems arising from the discretization of elliptic partial differential equations is one of the most persistent computational bottlenecks in scientific computing, and among these the Poisson equation is particularly ubiquitous. It governs electrostatic and gravitational potentials, steady-state diffusion and heat conduction, and the pressure field of incompressible flows, and it also arises as an inner subproblem in a wide range of larger simulation workflows.

Discretizing the equation on a grid with N unknowns often yields a large, sparse, and structured linear system $A\boldsymbol{x} = \boldsymbol{b}$, which in many applications must be solved repeatedly, at every time step of a transient simulation, for instance. The cumulative cost of these elliptic solves can therefore constitute a significant fraction of the total simulation cost. Computational fluid dynamics (CFD) provides a demanding and representative instance: incompressible flow solvers built on projection methods solve an elliptic pressure system at every time step, and the burden of high-fidelity flow simulation is severe enough that community roadmaps have identified quantum computing as a long-term research direction worth pursuing [1, 2].

The theoretical foundation for quantum linear solving was laid by the Harrow–Hassidim–Lloyd (HHL) algorithm [3], which establishes the possibility of an exponential speedup over classical methods for sparse, well-conditioned systems under idealized assumptions on sparsity, condition number, and data access. While HHL has been demonstrated experimentally on small systems [4], practical implementations remain challenging because it requires deep circuits and fault-tolerant hardware [5–7]. Similar limitations apply to the Quantum Singular Value Transformation (QSVT) [8], which provides a unified framework for matrix inversion, Hamiltonian simulation, and related linear algebra operations [9]. For the near-term Noisy Intermediate-Scale Quantum (NISQ) era [10], the Variational Quantum Linear Solver (VQLS) [11] has emerged as the most practically accessible alternative. VQLS recasts $A\boldsymbol{x} = \boldsymbol{b}$ as a variational optimization problem: a classical optimizer iteratively updates the parameters $\boldsymbol{\theta}$ of a parametrized quantum circuit $V(\boldsymbol{\theta})$ so as to minimize a cost function quantifying the mismatch between $A\,|x(\boldsymbol{\theta})\rangle$ and $|b\rangle$. The approach requires only shallow parametrized circuits and classical post-processing, and it has been explored for several elliptic systems including heat conduction [12, 13] and the Poisson equation [14].

Two obstacles have limited the practical reach of VQLS on discretized PDE systems. The first is the cost of encoding the operator. In the standard formulation [11], A must be expressed as a linear combination of L unitaries (LCU), and the cost function is estimated from $\mathcal{O}(L^2)$ independent Hadamard-test circuits. For the two-dimensional finite-difference Laplacian with a Pauli-LCU [15], the number of circuits required per cost-function evaluation grows exponentially in the qubit count $n = \log_2 N$ (Section III A). Thus, whatever compression the quantum state representation provides is forfeited at the level of circuit count alone. The second obstacle is trainability. VQLS optimization is affected by barren plateaus [16], in which the variance of the cost-function gradient decays exponentially with number of qubits, making it exponentially unlikely to sample a parameter configuration with a non-negligible gradient [16, 17]. In practice this manifests as an optimizer that appears to make no progress despite continued circuit evaluations.

A further and more fundamental caveat applies to quantum linear solvers generally: the solution is produced as a quantum state $|x\rangle$, and extracting the full classical solution vector requires $\mathcal{O}(N)$ measurements, which eliminates any potential exponential speedup [18]. Practical advantage therefore requires either that the work-

* Contact author:virajdanieldsouza@gmail.com
† aysinghal06@gmail.com
‡ alex.khan@bqpsim.com

flow be restructured to query low-dimensional functionals of the solution like forces, fluxes, energy norms, rather than the full field, or that the linear solver be embedded in a larger quantum pipeline that never requires classical readout. Both directions remain open, and the present work does not resolve them.

The block encoding [8] technique offers a route around the first obstacle. Efficient constructions for structured and sparse matrices have been explored [19–21], but their consequences for VQLS have not been systematically characterized. This paper develops block-encoded VQLS as a solver in its own right and characterizes it empirically. The block encoding is the unified construction for discrete Laplacian operators, a companion contribution by the authors [21], which supports Dirichlet, Neumann, Robin and periodic boundary conditions across arbitrary spatial dimensions within a single modular circuit, achieving an exact $(1, m, 0)$-block encoding with $m = 3 + \lceil \log_2 D \rceil$ ancilla qubits in D dimensions and gate complexity $\mathcal{O}(\log N \cdot \log D)$.

The second obstacle, trainability, is addressed empirically in this work. We characterize the barren plateau directly by measuring the decay of $\mathrm{Var}_{\boldsymbol{\theta}}[\partial_\mu C_G]$ with qubit number, and then examine the Covariance Matrix Adaptation Evolution Strategy (CMA-ES) [22, 23] as an alternative to COBYLA. CMA-ES is a population-based, derivative-free optimizer that adapts the full covariance matrix of its search distribution, enabling it to locate and follow narrow descent directions in high-dimensional flat landscapes. Across system sizes from $N = 4$ to $N = 1024$ we find that it delays the onset of stagnation and remains effective in regimes where COBYLA makes no progress, and that the parameter regions it visits carry gradient variances substantially above those of uniformly sampled parameters.

Our VQLS methodology is assessed on three benchmarks. The first is a Poisson problem with smooth sinusoidal forcing. The second is a steady-state heat conduction problem with a localized Gaussian source, modelling a heat-generating component embedded in a conducting plate. Both carry Dirichlet boundary conditions and are solved in isolation; the sinusoidal case admits an analytical solution and therefore provides a controlled accuracy check. The third places the solver inside a projection-method incompressible Navier–Stokes loop for the two-dimensional lid-driven cavity, where it is invoked once per time step on a Neumann system whose right-hand side changes as the flow evolves. This last case tests whether the attainable accuracy suffices to sustain a time-advancing simulation. All three are classically tractable and therefore furnish references against which the quantum solution can be measured.

The remainder of this paper is structured as follows. Section II presents the discretized 2D Poisson problem for Dirichlet and Neumann boundary conditions, develops the corresponding block-encoding circuits, and sets out the VQLS methodology. Section III reports the numerical results: the exactness and post-selection success probability of the encoding, circuit cost relative to the Pauli-LCU VQLS formulation, solution accuracy on the three benchmark problems, followed by characterization of the barren plateau and the effect of optimizer choice. Section IV summarises the findings and outlines directions for future work.

II. VQLS VIA BLOCK ENCODING: THEORY AND METHODOLOGY

A. The 2D Pressure-Poisson Problem

In incompressible CFD, projection and fractional-step methods [24, 25] enforce the divergence-free condition on the velocity field by solving a pressure-Poisson equation of the form

$$\nabla^2 p = \frac{\rho}{\Delta t} \nabla \cdot \mathbf{u}^*, \tag{1}$$

where $\mathbf{u}^*$ is the intermediate (non-solenoidal) velocity field, ρ is the fluid density (taken as unity throughout), and Δt is the time step. The right-hand side represents the local divergence error introduced during the velocity prediction step, and solving (1) yields the pressure correction that restores incompressibility [26]. This elliptic subproblem is one of the dominant computational bottlenecks in many CFD workflows, and it is therefore a natural and well-studied benchmark for linear solvers.

For the first two benchmark problems, we isolate the elliptic subproblem and consider the general two-dimensional Poisson equation on the unit square with homogeneous Dirichlet boundary conditions,

$$-\nabla^2 u(x, y) = f(x, y), \quad (x, y) \in [0, 1]^2, \qquad u\big|_{\partial\Omega} = 0, \tag{2}$$

where u is the unknown scalar field and f is a prescribed source term. Depending on the physical application, u may represent a pressure field arising from an incompressible flow projection step or a temperature field arising from steady-state heat conduction. The specific source terms used to benchmark the VQLS solver in this work are described in Section III.

The unit square is discretized on a uniform Cartesian grid with N_x interior points along x and N_y interior points along y, with uniform mesh spacings $\Delta x = 1/(N_x + 1)$ and $\Delta y = 1/(N_y + 1)$. Dirichlet boundary conditions are imposed on all four domain boundaries. As a result, only the $N = N_x \times N_y$ interior grid points are treated as unknowns. Applying a standard second-order central finite-difference stencil to the interior nodes yields the linear system

$$A\,\mathbf{x} = \mathbf{b}, \tag{3}$$

where $\mathbf{x} \in \mathbb{R}^N$ contains the interior field unknowns, and $\mathbf{b} \in \mathbb{R}^N$ contains the discretized forcing term together with any boundary contributions arising from the finite-difference stencil. The system matrix $A \in \mathbb{R}^{N\times N}$ inherits the separable Kronecker-sum structure of the Laplacian operator,

$$A = I_{N_y} \otimes T_{N_x} + T_{N_y} \otimes I_{N_x}, \tag{4}$$

where I_{N_d} denotes the $N_d \times N_d$ identity matrix and $T_{N_d} \in \mathbb{R}^{N_d \times N_d}$ is the standard one-dimensional second-order finite-difference Laplacian,

$$T_{N_d} = \frac{1}{(\Delta x_d)^2} \begin{pmatrix} -2 & 1 & & \\ 1 & -2 & 1 & \\ & \ddots & \ddots & \ddots \\ & & 1 & -2 \end{pmatrix} \in \mathbb{R}^{N_d \times N_d}. \tag{5}$$

Here $\Delta x_d = \{\Delta x, \Delta y\}$ based on the d involved. The matrix A is sparse and symmetric. Its sparsity pattern reflects the standard five-point finite-difference stencil connecting each interior node to its four nearest neighbours. In the present implementation, the negative sign associated with the continuous Poisson operator is absorbed into the right-hand side vector.

We also consider the pressure-Poisson equation (1) posed in a closed domain with impermeable walls, as in the lid-driven cavity considered in Section III. For the Neumann case the unknowns are placed at cell centres, $x_i = (i - \frac{1}{2})\Delta x$ with $\Delta x = 1/N_x$, rather than at the interior vertices of the Dirichlet grid. Imposing $\partial p/\partial n = 0$ through the ghost-node relation $p_{-1} = p_0$ modifies only the first and last rows of each one-dimensional factor, leaving the Kronecker-sum structure of (4) intact,

$$A^{\mathrm{N}} = I_{N_y} \otimes T^{\mathrm{N}}_{N_x} + T^{\mathrm{N}}_{N_y} \otimes I_{N_x}, \tag{6}$$

with the one-dimensional Neumann operator

$$T^{\mathrm{N}}_{N_d} = \frac{1}{(\Delta x_d)^2} \begin{pmatrix} -1 & 1 & & \\ 1 & -2 & 1 & \\ & \ddots & \ddots & \ddots \\ & & 1 & -1 \end{pmatrix}. \tag{7}$$

Comparing (7) with (5), the sole difference is the diagonal entry at the two boundary nodes, reduced from -2 to -1. Two properties of A^{N} (here the superscript N is a label for Neumann) bear on the quantum solve. It is singular, with null space spanned by the constant vector $\mathbf{1}$, so the solution is determined only up to an additive constant; we fix this gauge by projecting the recovered field onto the zero-mean subspace, which leaves ∇p and hence the corrected velocity unchanged. A solution exists provided the data are compatible, $\mathbf{1}^\top \boldsymbol{b} = 0$, which holds for the pressure system provided the normal velocity component of $\mathbf{u}^*$ vanishes on every wall face entering the discrete divergence. [26]

Both operators have spectral norm growing as $\mathcal{O}(1/h^2_{\min})$ with $h_{\min} = \min(\Delta x, \Delta y)$, whereas block encoding requires a matrix of spectral norm at most unity. The system must therefore be rescaled. The particular scaling used here is dictated by the structure of the encoding and is introduced in Section II B.

We consider a range of proof-of-concept discretization sizes spanning from $N = 4$ to $N = 1024$ interior unknowns, corresponding to uniform grids ranging from 2×2 to 32×32 interior points. These problem sizes are intentionally modest and are chosen to remain compatible with the qubit and circuit-depth limitations of current quantum simulators. In all cases, the classical reference solution is obtained using the Successive Over-Relaxation (SOR) iterative method, against which the VQLS solution is compared to assess solution accuracy.

B. Block Encoding of the 2D Laplacian

Block encoding provides the standard mechanism for embedding a generally non-unitary matrix into a larger unitary operator that can be realised as a quantum circuit. Formally, a unitary $U_A \in \mathbb{C}^{2^{n+m} \times 2^{n+m}}$ acting on m ancilla qubits and n system qubits is called an (α, m, ε)-block encoding of $A \in \mathbb{C}^{2^n \times 2^n}$ if

$$\left\| A - \alpha \big(\langle 0|^{\otimes m} \otimes I \big)\, U_A \left(|0\rangle^{\otimes m} \otimes I \right) \right\|_2 \leq \varepsilon, \tag{8}$$

where $\alpha > 0$ is the sub-normalization factor and $\varepsilon \geq 0$ is the approximation error. When $\varepsilon = 0$ the encoding is said to be *exact*. In block-matrix form, U_A takes the structure

$$U_A = \begin{pmatrix} A/\alpha & * \\ * & * \end{pmatrix}, \tag{9}$$

where the asterisks denote irrelevant blocks. Post-selecting the ancilla register on the outcome $|0\rangle^{\otimes m}$ projects the system register onto a state proportional to $A|\psi\rangle$, with success probability $\|A|\psi\rangle\|^2/\alpha^2$.

The block-encoding requirement $\|A\|_2 \leq 1$ is not satisfied by the system matrix A introduced in (4), whose spectral norm grows as $\mathcal{O}(1/h^2_{\min})$. We therefore introduce the globally scaled 2D Dirichlet Laplacian

$$\widetilde{A} := \frac{\Lambda}{4} A, \qquad \Lambda := \left(\frac{1}{\Delta x^2} + \frac{1}{\Delta y^2} \right)^{-1}, \tag{10}$$

which satisfies $\|\widetilde{A}\|_2 \leq 1$ by construction. The Kronecker-sum structure of (4) is preserved under this scaling, giving

$$\widetilde{A} = \omega_1\, \widetilde{A}^{(N_x)} \otimes I_{N_y} + \omega_2\, I_{N_x} \otimes \widetilde{A}^{(N_y)}, \tag{11}$$

where $\widetilde{A}^{(N_d)} := \frac{\Delta x_d^2}{4} T_{N_d}$ is the scaled 1D component along dimension d, satisfying $\|\widetilde{A}^{(N_d)}\|_2 \leq 1$, and the dimension-dependent weights

$$\omega_1 = \frac{1/\Delta x^2}{1/\Delta x^2 + 1/\Delta y^2}, \qquad \omega_2 = 1 - \omega_1, \tag{12}$$

satisfy $\omega_1 + \omega_2 = 1$. The linear system to be solved by VQLS is accordingly $\widetilde{A}\,\mathbf{x} = \widetilde{\mathbf{b}}$, where $\widetilde{\mathbf{b}} = (\Lambda/4)\,\mathbf{b}$. For a uniform grid, $\Delta x = \Delta y$, hence we get $\omega_1 = \omega_2 = 1/2$.

We employ the unified construction of [21] to build an explicit quantum circuit that block encodes $\widetilde{A}$. The construction exploits the Kronecker-sum separability of (11) by introducing a one-qubit *selector* register $|k\rangle$ that is prepared in the superposition

$$U_{\mathrm{prep}_k}|0\rangle = \sqrt{\omega_1}|0\rangle + \sqrt{\omega_2}|1\rangle, \tag{13}$$

implemented by a single $R_y(\theta_0)$ rotation with $\theta_0 = 2\arccos\sqrt{\omega_1}$. Conditioned on $|k\rangle = |d\rangle$ ($d \in \{1,2\}$), a one-dimensional block-encoding sub-circuit U_d for the boundary condition imposed along axis d is applied to the system register $|j^{(d)}\rangle$, after which $U^\dagger_{\mathrm{prep}_k}$ uncomputes the selector. This selector construction is independent of the boundary condition; only the one-dimensional sub-circuits differ. We describe the Dirichlet and Neumann sub-circuits in turn, and we note that the same scaling $\|\widetilde{A}^{(N_d)}\|_2 \le 1$ holds in both cases, since the spectrum of $T^{\mathrm{N}}_{N_d}$ likewise lies in $[-4/\Delta x_d^2, 0]$.

1. Dirichlet boundary conditions

Each 1D sub-circuit U_d is itself constructed from cyclic shift operators $S^-|j\rangle = |j-1 \bmod N_d\rangle$ and $S^+|j\rangle = |j+1 \bmod N_d\rangle$, a Hadamard–$Z$–Hadamard ladder on two ancilla qubits $|\ell_0\rangle$, $|\ell_1\rangle$, and one additional $|\mathrm{del}\rangle$ ancilla that suppresses the unwanted wrap-around coupling at the Dirichlet boundaries $j = 0$ and $j = N_d - 1$; see [21] for the full construction and proof.

The complete circuit, shown in Figure 1, uses $m = 4$ ancilla qubits in total and constitutes an exact $(1, 4, 0)$-block encoding of $\widetilde{A}$.

Following the analytical resource estimates of [21], the T-gate count of the 2D Dirichlet block-encoding circuit scales as $\mathcal{O}(\log N \cdot \log D)$, which for fixed dimension $D = 2$ reduces to $\mathcal{O}(\log N)$. This poly-logarithmic scaling in the matrix dimension is the central efficiency property of the construction.

2. Neumann boundary conditions

The pressure-Poisson system of Section II A carries homogeneous Neumann conditions on all four walls, and the corresponding scaled operator $\widetilde{A}^{\mathrm{N}}$ differs from the Dirichlet operator only in the boundary rows of each one-dimensional factor. The framework of [21] accommodates this case within the same circuit template. Dirichlet closure controls as shown in Figure 1 deletes the two wrap-around contributions of the cyclic shifts; Neumann closure additionally deletes one of the two diagonal branches at $j = 0$ and $j = N - 1$, which is precisely what reduces the boundary diagonal from -2 to -1 in (6). This costs two further comparator-controlled X gates, shown in Figure 2a, and the encoding remains exact. See [21] for the full construction and proof.

The two-dimensional Neumann block encoding is assembled by the same selector construction used in the Dirichlet case. Writing U_1^{N} and U_2^{N} for the one-dimensional sub-circuits of Figure 2a acting on the registers $|j^{(0)}\rangle$ and $|j^{(1)}\rangle$, Figure 2b shows the circuit in compact form.

C. Cost Function Evaluation and Solution Recovery

Given the scaled linear system $\widetilde{A}\mathbf{x} = \widetilde{\mathbf{b}}$, VQLS seeks a quantum state proportional to the solution vector by preparing a parametrized ansatz state

$$|x(\boldsymbol{\theta})\rangle = V(\boldsymbol{\theta})|0\rangle^{\otimes n}, \tag{14}$$

where $V(\boldsymbol{\theta})$ is a parametrized unitary circuit acting on n system qubits and $\boldsymbol{\theta} \in \mathbb{R}^p$ is the vector of variational parameters to be optimised. The goal is to find $\boldsymbol{\theta}^*$ such that $|x(\boldsymbol{\theta}^*)\rangle \propto \widetilde{A}^{-1}|\widetilde{b}\rangle$, where $|\widetilde{b}\rangle = U|0\rangle^{\otimes n}$ is the normalized right-hand side state prepared by a unitary U [27]. To drive the optimization towards this target, one needs a scalar cost function $C_G(\boldsymbol{\theta})$ that is (i) efficiently computable on a quantum circuit, (ii) equal to zero if and only if $\widetilde{A}|x(\boldsymbol{\theta})\rangle \propto |\widetilde{b}\rangle$, and (iii) positive otherwise.

A natural candidate is the normalized global cost function [11]

$$C_G(\boldsymbol{\theta}) = 1 - \frac{\left|\langle\widetilde{b}|\widetilde{A}|x(\boldsymbol{\theta})\rangle\right|^2}{\langle x(\boldsymbol{\theta})|\widetilde{A}^\dagger\widetilde{A}|x(\boldsymbol{\theta})\rangle}, \tag{15}$$

which measures the squared overlap between the normalized vectors $\widetilde{A}|x(\boldsymbol{\theta})\rangle/\|\widetilde{A}|x(\boldsymbol{\theta})\rangle\|$ and $|\widetilde{b}\rangle$. By the Cauchy–Schwarz inequality, $C_G(\boldsymbol{\theta}) \ge 0$ always holds. Moreover, $C_G(\boldsymbol{\theta}) = 0$ if and only if $\widetilde{A}|x(\boldsymbol{\theta})\rangle$ is proportional to $|\widetilde{b}\rangle$, i.e. if and only if $|x(\boldsymbol{\theta})\rangle \propto \widetilde{A}^{-1}|\widetilde{b}\rangle$, which is the desired solution state. Minimising $C_G(\boldsymbol{\theta})$ therefore directly drives the ansatz state towards the solution of the linear system. An equivalent and more convenient expression is obtained by recognising that the denominator is simply $\|\widetilde{A}|x(\boldsymbol{\theta})\rangle\|^2$, so that the cost can be written as

$$C_G(\boldsymbol{\theta}) = 1 - \left|\langle\widetilde{b}|\frac{\widetilde{A}|x(\boldsymbol{\theta})\rangle}{\|\widetilde{A}|x(\boldsymbol{\theta})\rangle\|}\right|^2 = 1 - |\langle 0^n|\Psi_{\mathrm{post}}(\boldsymbol{\theta})\rangle|^2\,, \tag{16}$$

where the post-selected state $|\Psi_{\mathrm{post}}(\boldsymbol{\theta})\rangle$ is defined in (22) below. The cost is therefore the complement of the fidelity between the normalized state $\widetilde{A}|x(\boldsymbol{\theta})\rangle$ and the target $|\widetilde{b}\rangle$: it equals zero at the solution and increases monotonically as the ansatz deviates from it.

In the block-encoding formulation [13], we assume the $(\alpha, m, 0)$-block-encoding unitary $U_{\widetilde{A}}$ of Section II B, with $\alpha = 1$ and $m = 4$ ancilla qubits for the discrete 2D Laplacian operator. The extended Hamiltonian operator is defined as,

$$H_G^{(\mathrm{ext})} := U^\dagger_{\widetilde{A}}\Big(|0^m\rangle\langle 0^m|_a \otimes \big(I_s - |\widetilde{b}\rangle\langle\widetilde{b}|_s\big)\Big)U_{\widetilde{A}}, \tag{17}$$

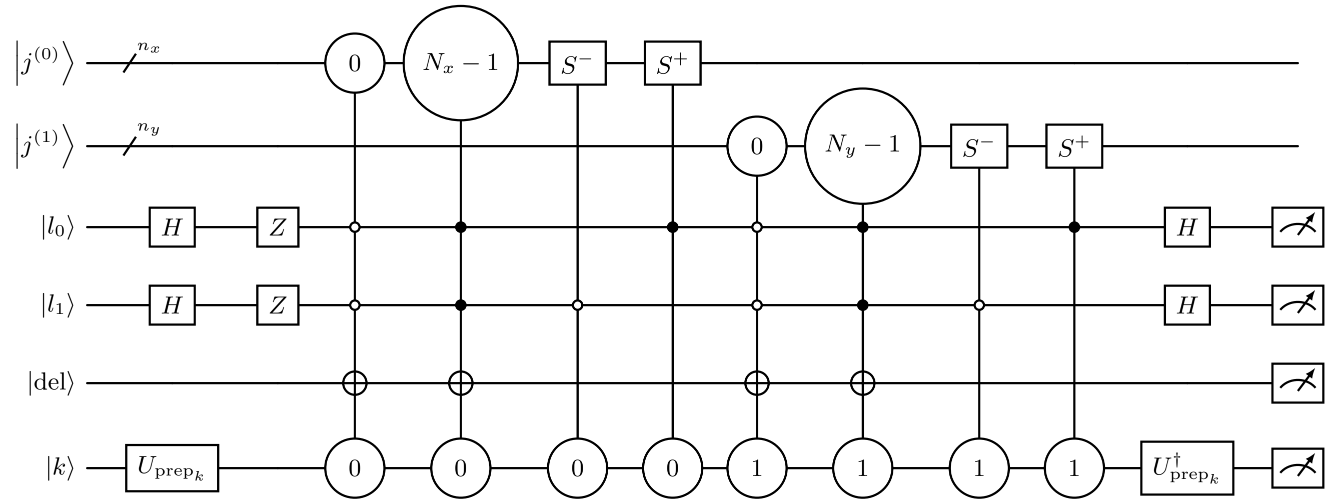

FIG. 1: Block encoding circuit for the 2D Laplacian with Dirichlet boundary conditions along both spatial directions, following the construction of [21]. Post-selecting all four ancilla qubits on $|0\rangle^{\otimes 4}$ realises the action of $\widetilde{A}$ on the system register.

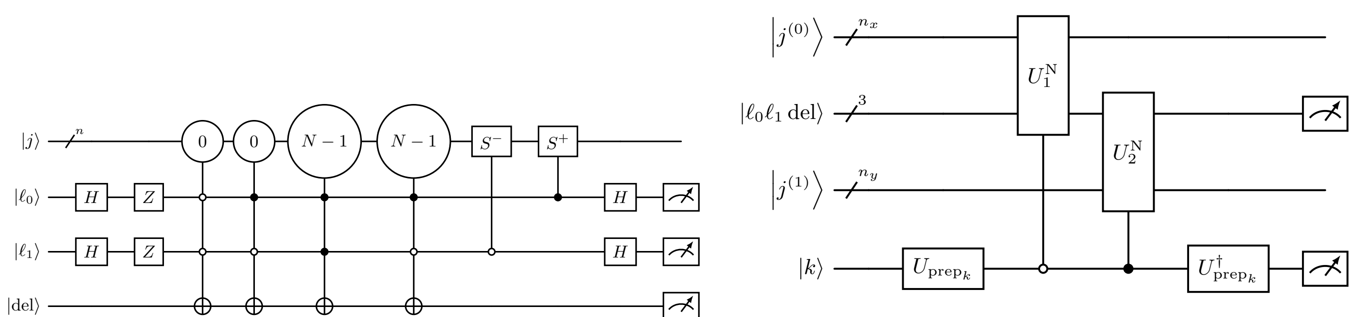

(a) One-dimensional Neumann sub-circuit U_d^{N}.

(b) 2D Laplacian with Neumann boundary conditions along both spatial directions

FIG. 2: Block-encoding circuits for the Laplacian with Neumann boundary conditions [21]. In (b), U_1^{N} and U_2^{N} denote the sub-circuit of (a) applied to the x- and y-registers. Post-selecting all four ancilla qubits on $|0\rangle^{\otimes 4}$ realises the action of $\widetilde{A}^{\mathrm{N}}$.

where the subscripts a and s refer to the ancilla and system subspaces respectively. For the input state $|X_{\mathrm{ext}}\rangle = |0^m\rangle_a \otimes |x(\boldsymbol{\theta})\rangle_s$, the expectation value of this Hamiltonian is

$$\langle X_{\mathrm{ext}}|H_G^{(\mathrm{ext})}|X_{\mathrm{ext}}\rangle = \frac{1}{\alpha^2}\langle x(\boldsymbol{\theta})|\widetilde{A}^\dagger\big(I - |\widetilde{b}\rangle\langle\widetilde{b}|\big)\widetilde{A}|x(\boldsymbol{\theta})\rangle, \tag{18}$$

which corresponds to the numerator of $C_G(\boldsymbol{\theta})$ up to the factor α^{-2}. Evaluating this expectation value on a quantum circuit proceeds as follows. One prepares

$$|\Psi'(\boldsymbol{\theta})\rangle := U_{\widetilde{A}}\big(|0^m\rangle \otimes |x(\boldsymbol{\theta})\rangle\big), \qquad U|0^n\rangle = |\widetilde{b}\rangle, \tag{19}$$

and post-selects the ancilla register on $|0^m\rangle$, yielding the unnormalized system state

$$\big(\langle 0^m| \otimes U^\dagger\big)|\Psi'(\boldsymbol{\theta})\rangle = \frac{1}{\alpha}\, U^\dagger \widetilde{A}|x(\boldsymbol{\theta})\rangle. \tag{20}$$

The probability of obtaining the ancilla outcome $|0^m\rangle$ is

$$p(\boldsymbol{\theta}) = \frac{\langle x(\boldsymbol{\theta})|\widetilde{A}^\dagger \widetilde{A}|x(\boldsymbol{\theta})\rangle}{\alpha^2}, \tag{21}$$

and the normalized post-selected state is

$$|\Psi_{\mathrm{post}}(\boldsymbol{\theta})\rangle = \frac{U^\dagger \widetilde{A}|x(\boldsymbol{\theta})\rangle}{\sqrt{\langle x(\boldsymbol{\theta})|\widetilde{A}^\dagger \widetilde{A}|x(\boldsymbol{\theta})\rangle}}. \tag{22}$$

Substituting into (16) and using Bayes' theorem, the fidelity term becomes

$$\begin{aligned} |\langle 0^n|\Psi_{\mathrm{post}}(\boldsymbol{\theta})\rangle|^2 &= P(\mathrm{sys} = |0^n\rangle \mid \mathrm{anc} = |0^m\rangle) \\ &= \frac{P\big(|0\rangle^{\otimes(n+m)}\big)}{P\big(|0\rangle^{\otimes m}\big)}, \end{aligned} \tag{23}$$

so that the global cost function is entirely determined by two measurement probabilities obtainable from a single quantum circuit, and the final expression for the cost is

$$C_G(\boldsymbol{\theta}) = 1 - \frac{P\big(|0\rangle^{\otimes(n+m)}\big)}{P(|0\rangle^{\otimes m})}. \tag{24}$$

A key advantage of the block-encoding formulation is that $C_G(\boldsymbol{\theta})$ is estimated from the measurement statistics of a *single* quantum circuit via (24), with $m = 4$ for the 2D Dirichlet/Neumann Laplacian case. Post-selecting the ancilla register on $|0\rangle^{\otimes 4}$ and measuring all qubits yields the numerator and denominator of Eq. (24), from which $C_G(\boldsymbol{\theta})$ is computed classically. This contrasts with the LCU based VQLS formulation [11], which requires $\mathcal{O}(L^2)$ separate Hadamard-test circuits for computing the cost function. The schematic VQLS circuit implementing this evaluation is shown in Figure 3.

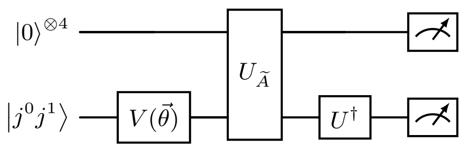

FIG. 3: Schematic VQLS circuit for the 2D Poisson problem via block encoding.

The VQLS optimization returns the normalized state $|x(\boldsymbol{\theta}^*)\rangle$ satisfying $\widetilde{A}|x(\boldsymbol{\theta}^*)\rangle \propto |\widetilde{b}\rangle$. It therefore encodes the direction of the solution but not its magnitude. Writing $\mathbf{x} = \|\mathbf{x}\|\,|x(\boldsymbol{\theta}^*)\rangle$ and substituting into (3) gives $A|x(\boldsymbol{\theta}^*)\rangle = \mathbf{b}/\|\mathbf{x}\|$; taking norms yields

$$\|\mathbf{x}\| = \frac{\|\mathbf{b}\|}{\sqrt{\langle x(\boldsymbol{\theta}^*)|A^\dagger A|x(\boldsymbol{\theta}^*)\rangle}}, \tag{25}$$

so that the classical solution vector is reconstructed as

$$\mathbf{x} = \frac{\|\mathbf{b}\|}{\sqrt{\langle x(\boldsymbol{\theta}^*)|A^\dagger A|x(\boldsymbol{\theta}^*)\rangle}}\,|x(\boldsymbol{\theta}^*)\rangle. \tag{26}$$

The quantity in the denominator is obtained coherently, from the post-selection statistics already collected during cost evaluation: by (21) and (10), $P(|0\rangle^{\otimes 4}) = (\Lambda/4)^2\langle x(\boldsymbol{\theta})|A^\dagger A|x(\boldsymbol{\theta})\rangle$, so that $\sqrt{\langle x(\boldsymbol{\theta}^*)|A^\dagger A|x(\boldsymbol{\theta}^*)\rangle} = (4/\Lambda)\sqrt{P(|0\rangle^{\otimes 4})}$ with Λ a known classical constant. Estimating it to relative precision ε costs $\mathcal{O}(1/(p\varepsilon^2))$ shots with p the post-selection success probability, independently of N, which is a further practical benefit of the improved success probability of the construction of [21].

For the variational circuit $V(\boldsymbol{\theta})$, we utilize the hardware-efficient ansatz (HEA) [28] comprising alternating single-qubit R_y rotation gates and two-qubit controlled-Z (CZ) entangling gates. Each layer consists of $R_y(\theta_i)$ rotations applied to all n system qubits, followed by CZ gates on alternating pairs of neighbouring qubits, followed by a second round of R_y rotations, as shown in the Figure 4. For an ansatz with l layers, the total number of variational parameters is $p = 2l(n-2)+n$, which scales linearly with the number of system qubits.

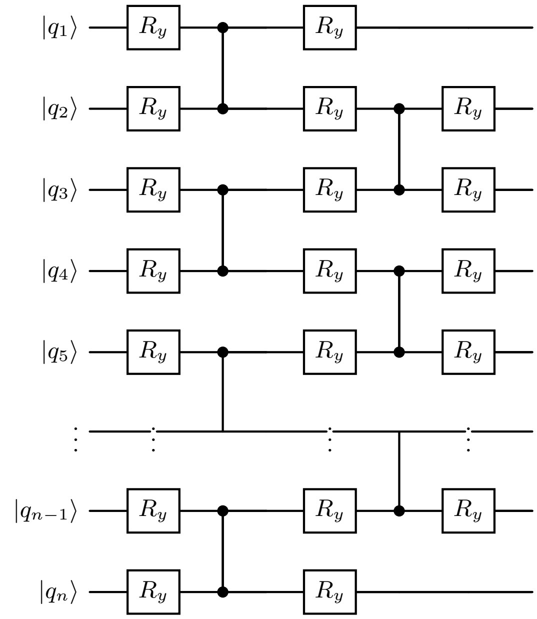

FIG. 4: Hardware-Efficient ansatz with one layer for $V(\vec{\theta})$.

D. The Barren-Plateau Phenomenon

A challenge shared by all variational quantum algorithms, VQLS included, is the barren-plateau phenomenon. As the number of qubits n or the circuit depth increases, the gradient of the cost function with respect to the variational parameters becomes exponentially suppressed. Formally, $C_G(\boldsymbol{\theta})$ exhibits a *probabilistic barren plateau* [16] if, for $\boldsymbol{\theta}$ sampled from some distribution,

$$\mathrm{Var}_{\boldsymbol{\theta}}[\partial_\mu C_G(\boldsymbol{\theta})] \in \mathcal{O}(b^{-n}), \tag{27}$$

for some $b > 1$ and some $\theta_\mu \in \boldsymbol{\theta}$: as n grows, the probability of sampling a parameter vector with a non-negligible gradient becomes exponentially small. The behaviour is attributed to the emergence of unitary 2-design characteristics in sufficiently deep or expressive circuits, and global cost functions of the form of (16) are known to be particularly susceptible [16, 29].

It is important to note, however, that barren plateaus describe an *average-case* property of the cost landscape rather than a uniform absence of gradients everywhere. Even in high-dimensional parameter spaces dominated by flat regions– narrow "gorges" [17], localized directions of non-negligible gradient magnitude can persist around the global minimum, but occupy an exponentially small fraction of the parameter space. Optimization success therefore depends less on the typical gradient magnitude than on whether the optimizer can find and stay within these atypical regions. Deterministic gradient-free methods relying on local differential information tend to stall once typical gradients are suppressed; on the contrary, population-based methods maintain broader exploration and may sample gorge-like directions that local models never see. Section III C tests this empirically, measuring (27) both under uniform sampling and along the trajectories the CMA-ES optimizer follows.

III. RESULTS

Section III A characterizes the block-encoding circuit itself: its exactness, its post-selection success probability, and its cost relative to the Pauli-LCU formulation of [11]. Section III B then reports solution accuracy on the three benchmark problems, and Section III C examines the barren plateau and the effect of optimizer choice. All simulations are performed on the Qiskit Aer statevector simulator. Classical reference solutions are obtained with the Successive Over-Relaxation (SOR) method applied to the identical discrete system. Because the variational optimization depends on the random initialization of $\boldsymbol{\theta}$, every configuration is run with five independent seeds; we report the geometric mean together with ± 1 standard deviation in $\log_{10}$ across seeds.

A. Circuit Verification and Resource Comparison

1. Exactness of the encoding

The construction of Section II B is an exact $(1, 4, 0)$-block encoding for both boundary conditions. Figure 5a verifies this directly by extracting the top-left block of the assembled circuit unitary and comparing it against the target operator. The deviation $\|(\langle 0^4| \otimes I)\, U_{\widetilde{A}}\, (|0^4\rangle \otimes I) - \widetilde{A}\|_\infty$ remains at the level of double-precision machine epsilon across the full range $N = 4$ to $N = 1024$, for the Dirichlet operator of the heat conduction benchmark and the Neumann operator of the lid-driven cavity alike.

2. Post-selection success probability

Evaluating $C_G(\boldsymbol{\theta})$ through (24) requires post-selecting the ancilla register on $|0\rangle^{\otimes 4}$, and only that fraction of shots contributes. Since estimating C_G to relative precision ε costs $\mathcal{O}(1/(p\varepsilon^2))$ shots, the scaling of p with system size determines whether the reduction to a single circuit translates into a genuine saving. Figure 5b reports $p(\boldsymbol{\theta}^*)$ at the optimized parameters. The decay is far slower than the N^{-2} behaviour that the shrinking spectral gap of the scaled Laplacian might suggest: fitting a power law gives $p \sim N^{-0.57}$ for the Dirichlet operator and $p \sim N^{-0.94}$ for the Neumann operator. The shot cost per cost-function evaluation therefore grows as $\mathcal{O}(N^{0.57})$ and $\mathcal{O}(N^{0.94})$ respectively, against $\Theta(N)$ circuits for the Pauli-LCU formulation, each of which itself requires $\mathcal{O}(1/\varepsilon^2)$ shots.

3. Comparison with the Pauli-LCU formulation

We compare against VQLS in the formulation of [11], in which the Dirichlet Laplacian is expanded in the Pauli basis and the cost function assembled from Hadamard tests. The comparison uses the heat conduction operator; the Neumann case behaves analogously and is omitted for brevity. For the LCU implementation we report, at each size, the resources of the most expensive circuit in the set, which bounds the per-circuit requirement.

The principal difference is the number of circuits. A Pauli decomposition of the 2D Dirichlet Laplacian yields exactly $L = N_x + N_y - 1$ terms, and the cost function requires $L(L+1)$ distinct Hadamard-test circuits per evaluation (Figure 6a). On a square grid this is $\Theta(N)$, growing from 12 circuits at $N = 4$ to 9120 at $N = 2048$, whereas the block-encoded formulation requires exactly one circuit at every size.

Per-circuit resources tell a more nuanced story. The block-encoded circuit carries four ancillae against one for the LCU circuits, so its width is larger by three qubits at every size. In gate count and depth the LCU circuits are individually cheaper at small and intermediate sizes, but the two constructions scale differently and the ordering reverses beyond $N = 512$ (Figures 6b and 6c). At $N = 1024$ the block-encoded circuit is already the shallower of the two, and the margin widens with system size: at $N = 4096$ it requires 16,034 two-qubit gates against 28,980 for the heaviest LCU circuit, at a depth of 28,741 against 45,744.

Taken together with the circuit count, the aggregate cost per cost-function evaluation, defined as the product of the number of circuits and the gate count per-circuit, differs by orders of magnitude and the gap widens monotonically with the size of the system. The block-encoded formulation is thus a cheaper construction on every axis except for a modest constant increase in width.

The Pauli decomposition is in one respect the most favourable LCU available: its per-circuit depth for the Hadamard test circuits used in VQLS is close to the minimum any linear-combination formulation can achieve. Its weakness is the term count, which forces $\Theta(N)$ circuit evaluations per cost function for the 2D Laplacian. More compact decompositions of the discrete Laplacian exist [30], reducing L at the cost of unitaries that are individually more expensive. Since the block-encoded circuit is already shallower than the Pauli-LCU circuit beyond $N = 512$, and any such decomposition has a per-circuit depth at least that of the Pauli case, the crossover against a compact LCU would be expected at a smaller system size.

B. Solution Accuracy

Three benchmark problems are considered. The first two are instances of the Dirichlet problem (2) and differ only in the source term; the third places the solver

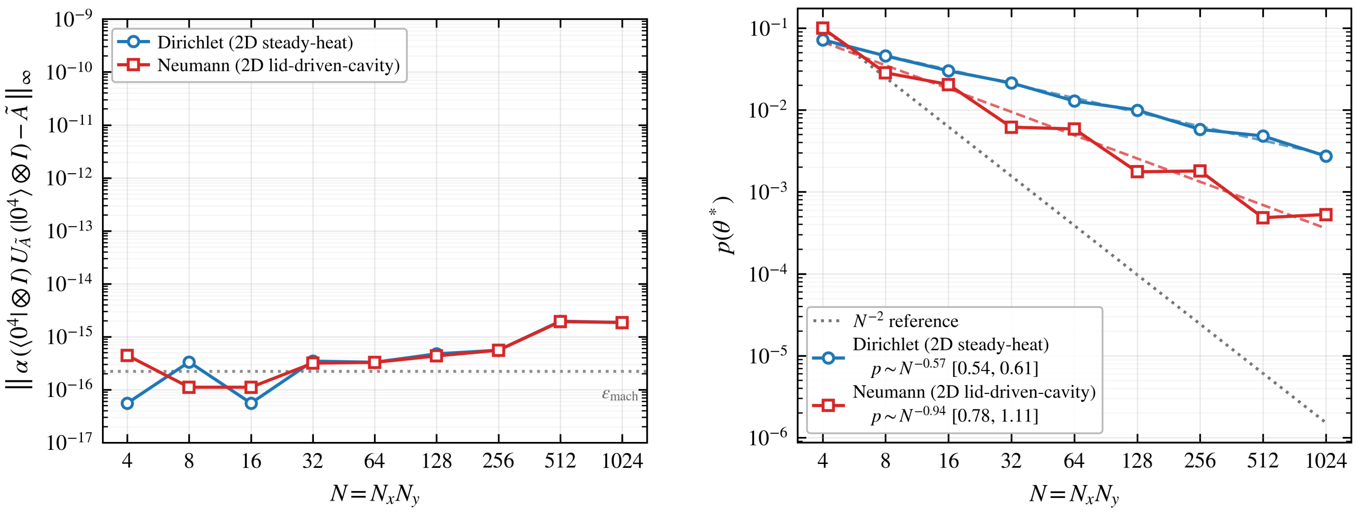

(a) Infinity-norm deviation of the compiled circuit's top-left block from the target operator; the dotted line marks double-precision machine epsilon.

(b) Post-selection success probability at the optimized parameters, with least-squares power-law fits $p \sim N^{-s}$ and 95% confidence intervals.

FIG. 5: Performance and numerical exactness of the block-encoding circuits used in this work.

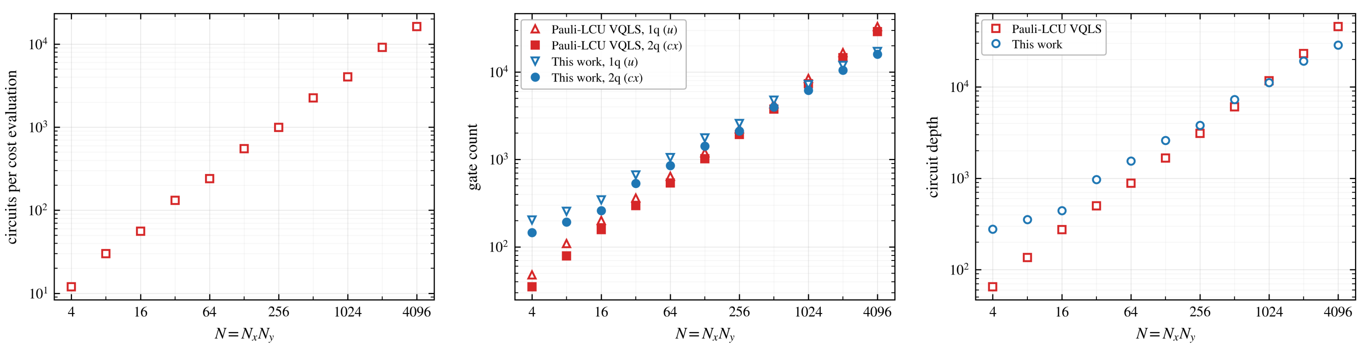

(a) Circuits per cost evaluation, Pauli-LCU.

(b) One- and two-qubit gate counts.

(c) Circuit depth.

FIG. 6: Resource comparison between the Pauli-LCU VQLS and the block-encoded formulation of this work, for the 2D Dirichlet Laplacian. (a) The block-encoded formulation requires one circuit at every size and is therefore not plotted. (b), (c) Per-circuit counts after transpilation to the $\{U, \mathrm{CX}\}$ basis; for the Pauli-LCU formulation these are for the most expensive Hadamard-test circuit at each grid, an empirical per-circuit upper bound.

inside a time-advancing flow simulation under Neumann boundary conditions. Accuracy is reported as the infidelity $1-F$ between the recovered and reference solution vectors, where $F = |\langle x^{\mathrm{SOR}}|x(\boldsymbol{\theta}^*)\rangle|^2$. All runs use CMA-ES optimizer with $\sigma_0 = 0.3$ and a population of 15 per generation, terminating at 6×10^4 generations or on a cost tolerance of 10^{-12}, whichever is reached first. The ansatz layers is $\ell = 3$ for $N \leq 256$ and $\ell = 5$ at $N = 512$ and $N = 1024$.

1. *Sinusoidal source*

The first benchmark takes the smooth source term

$$f(x, y) = -\sin(\pi x)\sin(\pi y), \tag{28}$$

with homogeneous Dirichlet conditions on all four walls. The forcing is smooth and free of singularities, and the problem admits the analytical solution $u(x, y) = \sin(\pi x)\sin(\pi y)/(2\pi^2)$.

Figure 7 shows the classical and VQLS solution fields on the 32×32 grid ($N = 1024$, $n = 10$ system qubits, 14 total), together with the cost-function history averaged over the five seeds. The VQLS solution reproduces the smooth bell-shaped distribution characteristic of the sinusoidal source, peaking at the domain centre and decaying to zero at the walls in accordance with the homogeneous Dirichlet conditions. Agreement is exact to arithmetic precision: the median seed attains $1 - F = 8.9 \times 10^{-16}$ at a final cost of $C_G = 4.7 \times 10^{-15}$, and all five seeds lie at the same level.

2. *Gaussian source*

The second benchmark is the steady-state heat conduction equation $-k\nabla^2 T = Q(x, y)$, an instance of (2) with $u \equiv T$ and a spatially localized source,

$$Q(x,y) = Q_0 \exp\left(-\frac{(x-x_0)^2 + (y-y_0)^2}{2\sigma^2}\right), \qquad (29)$$

with $Q_0 = 5$, $(x_0, y_0) = (0.5, 0.3)$ and $\sigma = 0.1$. The boundary conditions are Dirichlet throughout: the bottom wall is held at $T_{\text{hot}} = 1$, the top wall at $T_{\text{cold}} = 0$, and the side walls at the mean of the two. The configuration models a heat-generating component embedded in a conducting plate held between a hot base and a cold lid, and unlike the sinusoidal case it presents the solver with a sharp interior gradient superposed on a smooth background stratification.

Figure 8 shows the corresponding fields and cost history on the 32×32 grid. The VQLS field reproduces the vertical thermal stratification set by the hot and cold walls, but the isotherms are flattened relative to the classical reference. The median seed attains $1 - F = 4.4 \times 10^{-2}$ at a final cost of $C_G = 4.2 \times 10^{-3}$.

Table I summarises the accuracy attained on both Dirichlet benchmarks across the full range of system sizes. The two behave quite differently. The sinusoidal source is recovered to arithmetic precision at every size, which is expected once one notes that the discretized forcing is an exact eigenvector of the discrete Dirichlet Laplacian: the solution state coincides with $|b\rangle$, so the ansatz need only prepare a state of Schmidt rank one across the x–y register cut. This case therefore verifies the pipeline end to end. Fo the Gaussian source, the solution has an overlap of ≈ 0.78 with $|b\rangle$ at $N = 1024$. Its infidelity remains at arithmetic precision through $N = 32$, and rises for grid sizes beyond this. This can be attributed to the optimization which is discussed in Section III C.

3. *Lid-driven cavity*

Here we empirically examine, whether the accuracy attainable by the VQLS solver suffices to sustain a simulation in which the system is solved repeatedly, with a right-hand side that evolves as the solution does.

We take the two-dimensional lid-driven cavity, the standard validation case for incompressible flow solvers. Fluid occupies a square domain with no-slip conditions on all four walls, the upper wall translating at constant velocity U_{lid} and driving a recirculating vortex in the interior. The flow is advanced by the projection method of Section II A: at each time step an intermediate velocity field is predicted, the Neumann pressure-Poisson system (6) is solved to obtain the pressure correction, and the velocity is projected onto the divergence-free subspace [26]. The VQLS solver of Section II C is invoked once per time step in place of the classical pressure solve, using the Neumann block encoding of Section II B 2. Each step is warm started from the converged parameters of the previous step, so only the first solve begins from a random initialization. Because the recovered pressure enters the velocity correction directly, any error committed at one step is carried into the initial condition of the next.

The simulation is run on a 16×16 grid at $Re = 100$ with $\Delta t = 0.05$, giving a Neumann system of $N = 256$ unknowns ($n = 8$ system qubits). Because every time step requires a complete variational optimization, we advance ten steps to $t = 0.5$ and compare against the classical solver run. At this time the viscous diffusion length is $\sqrt{\nu t} \approx 0.07$, roughly one cell width, so the flow is still developing and far away from the steady-state.

Figure 9 shows the outcome. The streamline patterns are closely similar: both solvers place the primary vortex near $(x/L, y/L) \approx (0.6, 0.85)$ and reproduce the same recirculation structure. The centreline profiles quantify the difference. The discrepancy is systematic and the quantum pressure solve slightly damps the velocity magnitude while preserving the structure of the field.

Thus we observe that the two trajectories remain together over ten time steps. Each step feeds its pressure directly into the velocity correction, so an error committed at one step enters the initial condition of the next; a solver whose output were merely qualitatively correct would be expected to drift.

TABLE I: VQLS solution infidelity $1 - F$ across system sizes for both Dirichlet benchmarks, where $F = |\langle x^{\text{SOR}} | x(\boldsymbol{\theta}^*)\rangle|^2$. Entries are the geometric mean over five independent seeds, for CMA-ES with $\sigma_0 = 0.3$ at ansatz depth ℓ. n denotes system qubits; total circuit width is $n + 4$.

$N_x \times N_y$	N	n	ℓ	$1-F$ Sine	$1-F$ Heat
2×2	4	2	3	3.1×10^{-16}	3.0×10^{-16}
2×4	8	3	3	2.1×10^{-16}	1.1×10^{-15}
4×4	16	4	3	3.8×10^{-16}	1.8×10^{-15}
4×8	32	5	3	3.2×10^{-16}	1.5×10^{-15}
8×8	64	6	3	3.4×10^{-16}	3.2×10^{-5}
8×16	128	7	3	2.5×10^{-16}	1.4×10^{-3}
16×16	256	8	3	1.8×10^{-16}	3.8×10^{-2}
16×32	512	9	5	1.2×10^{-16}	3.8×10^{-2}
32×32	1024	10	5	2.0×10^{-15}	5.1×10^{-2}

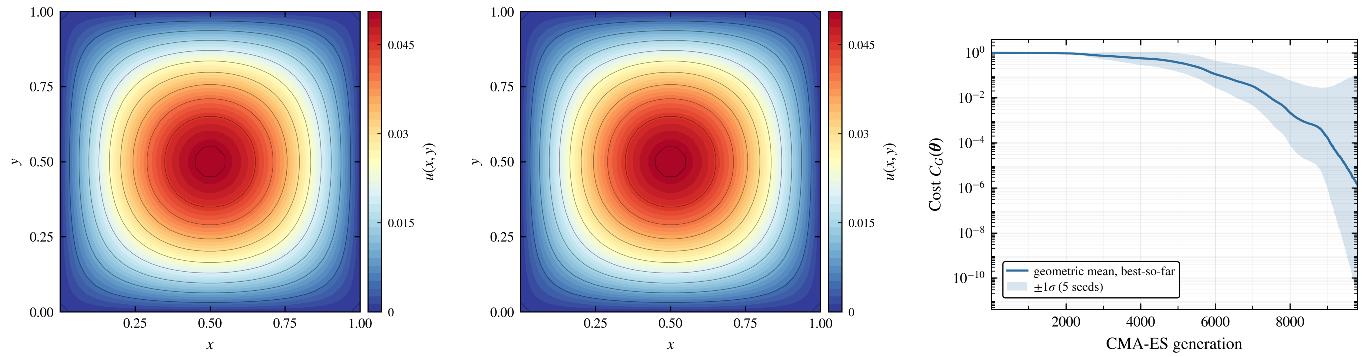

(a) Classical (SOR) solution. (b) VQLS solution, median seed. (c) Cost history over five seeds.

FIG. 7: Sinusoidal source benchmark on the 32×32 grid ($N = 1024$, $n = 10$ system qubits, 14 total), CMA-ES with $\sigma_0 = 0.3$ and $\ell = 5$ ansatz layers. Panels (a) and (b) share a colour scale and show the seed attaining the median infidelity of the five runs, $1 - F = 8.9 \times 10^{-16}$. In (c) the solid line is the geometric mean of the best-so-far cost across seeds and the band is ± 1 standard deviation in $\log_{10}$; the median seed reaches $C_G = 4.7 \times 10^{-15}$.

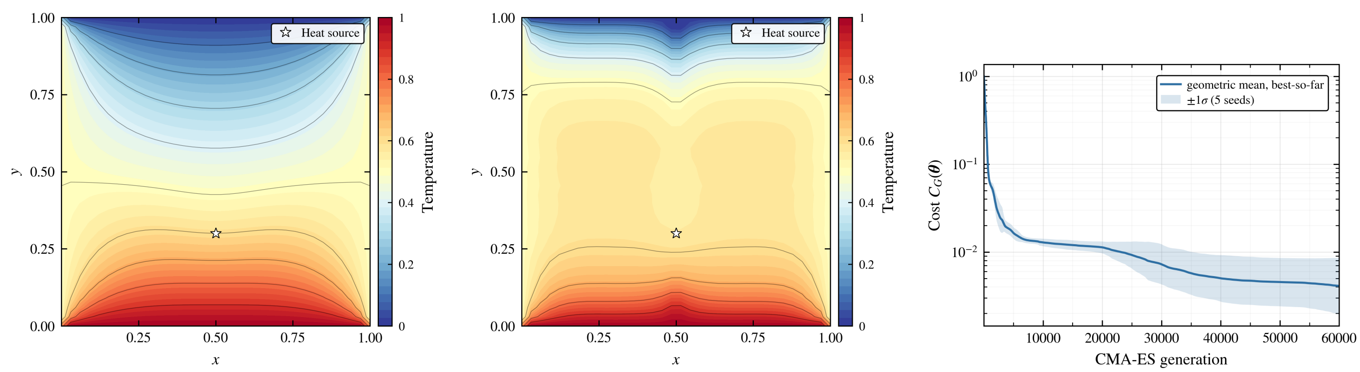

(a) Classical (SOR) solution. (b) Quantum (VQLS) solution. (c) Cost history over five seeds.

FIG. 8: Heat conduction benchmark with Gaussian source on the 32×32 grid ($N = 1024$, $n = 10$ system qubits, 14 total), CMA-ES with $\sigma_0 = 0.3$ and $\ell = 5$ ansatz layers. The star marks the source at $(x_0, y_0) = (0.5, 0.3)$. Panels (a) and (b) share a colour scale and show the seed attaining the median infidelity of the five runs, $1 - F = 4.4 \times 10^{-2}$. In (c) the solid line is the geometric mean of the best-so-far cost across seeds and the band is ± 1 standard deviation in $\log_{10}$; the median seed reaches $C_G = 4.2 \times 10^{-3}$.

C. Barren Plateaus and the Role of the Optimizer

The results of the 2D heat conduction problem degrade with system size as shown in Table I. The limitation lies in the optimization, and we examine it here in two steps: first establishing that the cost landscape exhibits a barren plateau in the sense of (27), then asking what distinguishes an optimizer that continues to make progress from one that does not.

1. *Gradient variance under uniform sampling*

Figure 10a reports $\mathrm{Var}_{\boldsymbol{\theta}}[\partial_\mu C_G]$, averaged over parameter indices μ, for $\boldsymbol{\theta}$ drawn uniformly from $[0, 2\pi)^d$, at ansatz depths $\ell = 2$ to 5 and system sizes $n = 2$ to 10. The decay is exponential in n at every depth, which is the defining signature of (27). Fitting $\mathrm{Var} \propto b^{-n}$ gives $b = 3.90$, 3.78, 3.77 and 3.95 for $\ell = 2$ to 5: statistically indistinguishable across depths. This is consistent with the plateau being a property of the global cost function (16) rather than of ansatz expressivity, the regime identified in [29].

2. *Gradient variance along the optimizer trajectory*

An optimizer concentrates its evaluations where it has found descent, and it is the gradient structure of those regions, not of the parameter space at large, that governs whether optimization proceeds. Figure 10b repeats the measurement with $\boldsymbol{\theta}$ drawn from the points CMA-ES actually visits over 100 generations. The variances are one to three orders of magnitude above the uniform baseline at every size, and the apparent decay rate varies strongly

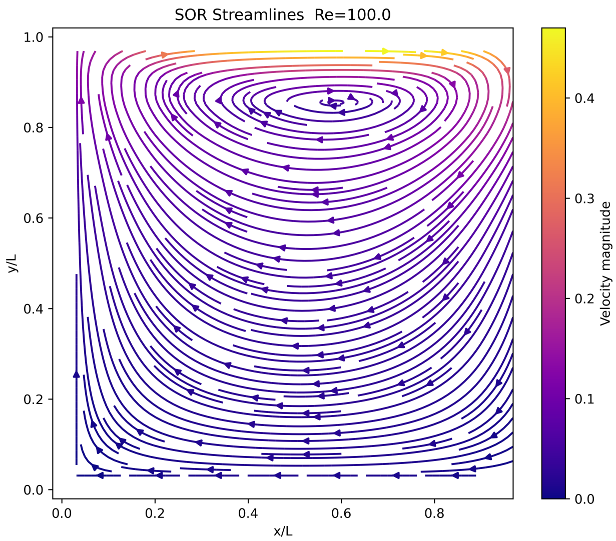

(a) Classical (SOR) streamlines.

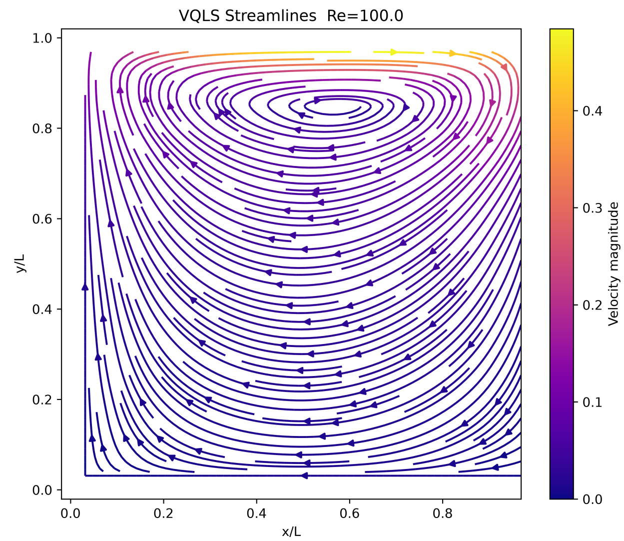

(b) VQLS streamlines.

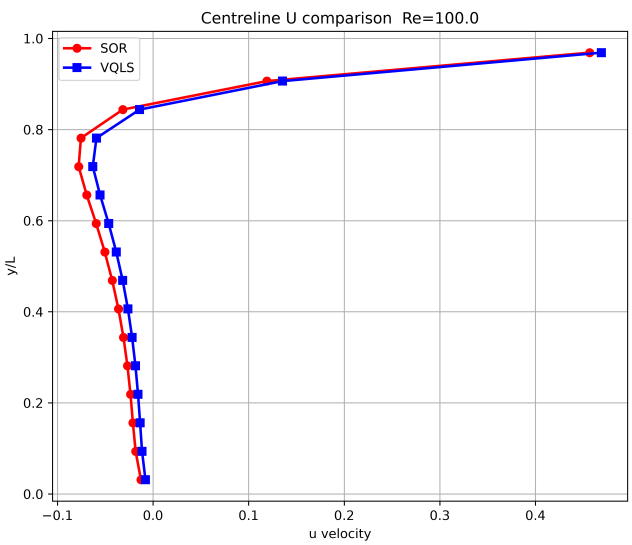

(c) u along the vertical centreline.

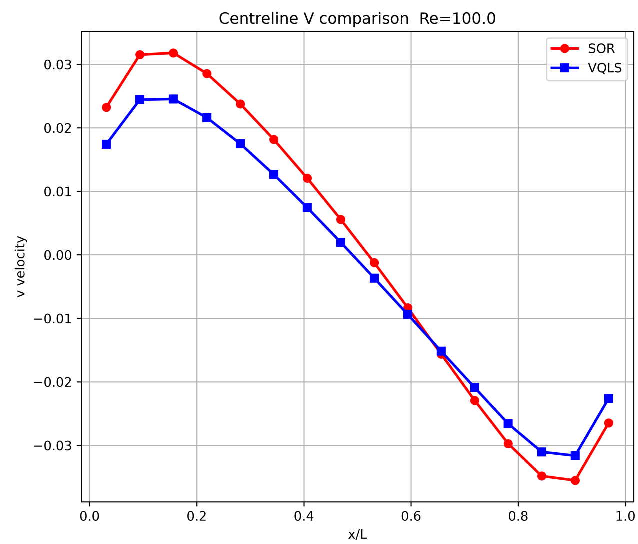

(d) v along the horizontal centreline.

FIG. 9: Lid-driven cavity at $Re = 100$ on a 16×16 grid, after ten steps of $\Delta t = 0.05$ ($t = 0.5$). The two solvers differ only in the pressure-Poisson solve; the discretization, initial condition and time step are identical. The flow is still developing at this time.

with depth, in contrast to the uniform sampling case.

We emphasize that this is an observation about where the optimizer goes, not a demonstration that its search strategy causes the effect: elevated gradient variance along a trajectory is in part a consequence of successful optimization as much as a cause of it. What the measurement does establish is that the regions CMA-ES occupies are atypical of the landscape as a whole, in exactly the manner the narrow-gorge picture of [17] anticipates, and that the exponential suppression of variance of cost gradient is substantially weaker along the path actually taken.

3. *Consequences for optimizer choice*

The practical question is whether this difference is visible in convergence behaviour, and in Figure 11, the two optimizers are compared at equal cost: a CMA-ES generation evaluates the cost function once per population member, so 4,000 generations at a population of 15 corresponds to the 6×10^4 evaluations allotted to COBYLA.

At $N = 1024$, COBYLA descends rapidly over the first few thousand evaluations and then flattens, making no further progress within its budget: its local linear model cannot identify productive descent directions once typical

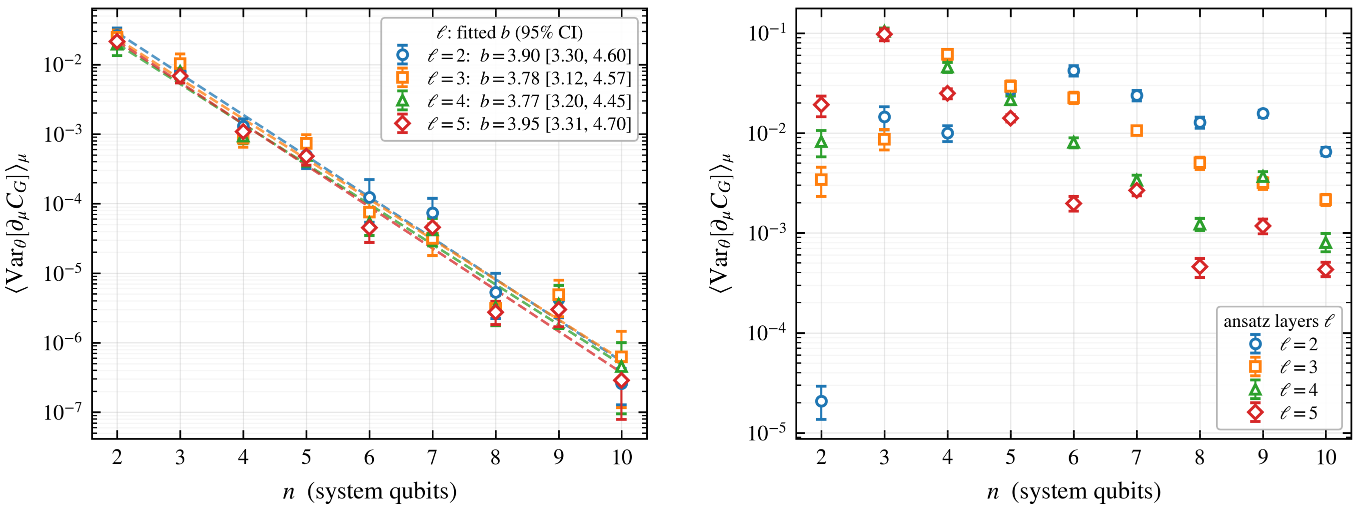

(a) Uniform sampling, $\boldsymbol{\theta} \sim U[0, 2\pi)^d$. Dashed lines are fits of Var $\propto b^{-n}$.

(b) Sampling along the CMA-ES trajectory. No fit is shown; see text.

FIG. 10: Variance of the global cost gradient against the number of system qubits n, at hardware-efficient ansatz depths $\ell = 2$ to 5. Each point averages the per-parameter variance over five randomly chosen parameters from 200 samples; error bars are 95% confidence intervals.

gradients are suppressed. CMA-ES continues to reduce the cost throughout.

A further practical difference is that for the population within a CMA-ES generation all cost evaluations are independent and can be run in parallel. COBYLA is inherently sequential, each iteration depending on the outcome of the last. This does not alter the number of circuit calls, and on a single quantum processor circuits execute serially in any case, but it is relevant wherever multiple devices or simulator instances are available.

It is important to note that CMA-ES does not remove the barren plateau which is fundamental to the cost landscape. It postpones the size at which stagnation sets in, which is what the difference between the two panels of Figure 10 would lead one to expect.

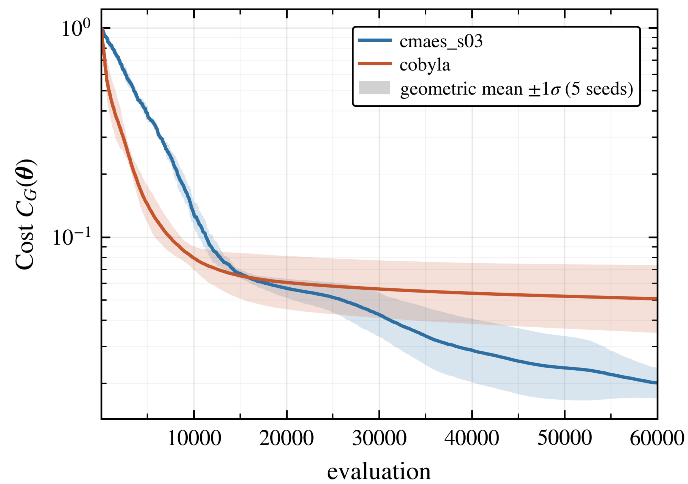

FIG. 11: Cost function convergence for COBYLA and CMA-ES on the heat conduction benchmark ($N = 1024$) at equal budget: 4,000 CMA-ES generations of population 15 against 6×10^4 COBYLA iterations, i.e. 6×10^4 cost-function evaluations each. Solid lines are the geometric mean of the best-so-far cost across five seeds; bands are ± 1 standard deviation in $\log_{10}$.

IV. CONCLUSION AND FUTURE WORK

We have developed a variational quantum linear solver for the discrete Poisson equation built on an exact block encoding of the Laplacian, and characterized it on three benchmarks.

The encoding reproduces the target operator to double-precision machine epsilon at every size from $N = 4$ to $N = 1024$, for Dirichlet and Neumann boundaries alike. Its post-selection success probability decays as $N^{-0.57}$ and $N^{-0.94}$ for the two boundary conditions, far more slowly than the N^{-2} that would cancel the advantage of reducing the cost function to a single circuit. Against the Pauli-LCU formulation, the difference is one of circuit count: the Pauli-LCU VQLS requires $\Theta(N)$ circuits per cost evaluation, against one in the block encoded VQLS. Per circuit the LCU is cheaper at small sizes, but the ordering reverses beyond $N = 512$ in both gate count and depth, at a fixed cost of three additional ancilla qubits.

Solution accuracy separates sharply between the two Dirichlet benchmarks, and the reason is instructive. The sinusoidal forcing is an exact eigenvector of the discrete Laplacian, so its solution state coincides with $|b\rangle$; the solver recovers it to arithmetic precision at every size, which verifies the pipeline end to end but does not probe its scaling. For the Gaussian source, the infidelity remains at machine precision through $N = 32$, then grows by roughly an order of magnitude per grid size increase.

That degradation is attributable to the optimization. Direct measurement confirms a barren plateau: the gradient variance under uniform sampling decays as b^{-n}, statistically indistinguishable across ansatz depths $\ell = 2$ to 5 and therefore driven by the growth of the Hilbert space rather than by circuit depth. Sampled instead along the CMA-ES trajectory, the variance is one to three orders of magnitude higher at every size. The regions the optimizer occupies are thus atypical of the landscape as a whole, which is consistent with its continuing to make progress at sizes where COBYLA stalls, though we do not claim a causal mechanism.

Embedded in a projection-method Navier–Stokes loop, the solver sustains a lid-driven cavity simulation at $Re = 100$ on a 16×16 grid, tracking the classical trajectory in both streamline structure and centreline profiles over ten time steps.

Several directions follow. On the encoding side, the construction extends without modification to mixed boundary conditions and to three or more spatial dimensions [21], and block encodings have been developed for non-uniform grids and non-Cartesian meshes [31]; both are needed before the approach can address realistic geometries. A quantitative comparison against compact, non-Pauli LCU decompositions would sharpen the resource argument made in Section III A. The block-encoding circuits used in this work are directly reusable as subroutines in Quantum Singular Value Transformation (QSVT)-based fault-tolerant quantum linear solvers [8], which is theoretically known to provide speedups over classical methods under well-defined conditions on matrix sparsity and condition number.

On the optimization side, the empirical advantage of CMA-ES lacks a theoretical account. Understanding why a covariance-adapting search locates and remains within the atypical regions identified here, and whether that behaviour persists as n grows, is the open question this work raises most directly. Related is the design of ansätze that exploit the sparsity and Kronecker-sum structure of the Laplacian rather than treating it as a generic operator.

The most promising path to practical quantum advantage and utility is to identify and efficiently obtain low-dimensional functionals of the solution rather than the full solution field, thereby circumventing the classical readout bottleneck. Identifying which quantities of engineering interest admit efficient quantum observable estimation is an important open problem that we intend to pursue in future work. Finally, all results reported here are from exact statevector simulation. This isolates the properties of the encoding and of the optimization landscape from sampling and hardware noise, but leaves the shot requirements and noise resilience of the method uncharacterized; the success-probability scaling of Section III A quantifies the former but does not substitute for measuring it. Establishing both is a prerequisite for any hardware demonstration.

ACKNOWLEDGMENTS

The authors thank Alexandre Boutot (University of Waterloo) for his contributions to the block-encoding framework in a companion work [21]. The authors also thank Rajas K. Dalvi for his insights on the role of optimizers in delaying barren plateaus, and Kunal Garg for reviewing the manuscript.

[1] A. W. Cary, J. Chawner, E. P. Duque, W. Gropp, W. L. Kleb, R. M. Kolonay, E. Nielsen, and B. Smith, CFD vision 2030 road map: Progress and perspectives, in *AIAA AVIATION 2021 Forum* (2021).

[2] M. Mani and A. J. Dorgan, A perspective on the state of aerospace Computational Fluid Dynamics technology, Annual Review of Fluid Mechanics **55**, 431 (2023).

[3] A. W. Harrow, A. Hassidim, and S. Lloyd, Quantum algorithm for linear systems of equations, Phys. Rev. Lett. **103**, 150502 (2009).

[4] Y. Zheng, C. Song, M.-C. Chen, B. Xia, W. Liu, Q. Guo, L. Zhang, D. Xu, H. Deng, K. Huang, Y. Wu, Z. Yan, D. Zheng, L. Lu, J.-W. Pan, H. Wang, C.-Y. Lu, and X. Zhu, Solving systems of linear equations with a superconducting quantum processor, Phys. Rev. Lett. **118**, 210504 (2017).

[5] IBM Quantum, IBM quantum technology roadmap, https://www.ibm.com/quantum/technology (2024).

[6] Quantinuum, Quantinuum accelerated roadmap to universal fault-tolerant quantum computing by 2030, https://www.quantinuum.com/press-releases (2024).

[7] IonQ, IonQ accelerated roadmap: Turning quantum ambition into reality, https://www.ionq.com/roadmap (2024).

[8] A. Gilyén, Y. Su, G. H. Low, and N. Wiebe, Quantum singular value transformation and beyond: Exponential improvements for quantum matrix arithmetics, in *Proceedings of the 51st Annual ACM SIGACT Symposium on Theory of Computing (STOC)* (ACM, 2019) pp. 193–204.

[9] J. M. Martyn, Z. M. Rossi, A. K. Tan, and I. L. Chuang, Grand unification of quantum algorithms, PRX Quantum **2**, 040203 (2021).

[10] J. Preskill, Quantum computing in the NISQ era and beyond, Quantum **2**, 79 (2018).

[11] C. Bravo-Prieto, R. LaRose, M. Cerezo, Y. Subaşı, L. Cincio, and P. J. Coles, Variational quantum linear solver, Quantum **7**, 1188 (2023).

[12] Y. Y. Liu, Z. Chen, C. Shu, S. C. Chew, B. C. Khoo, X. Zhao, and Y. D. Cui, Application of a variational

hybrid quantum-classical algorithm to heat conduction equation and analysis of time complexity, Physics of Fluids **34**, 117121 (2022).

[13] V. D'Souza, S. Dhamotharan, T. Kumar, R. Kolluru, F. D. Bosco, A. Chopra, R. Lineswala, and O. Sahni, Towards hybrid quantum-classical computing for large-scale CFD: Tackling scalability challenges of the variational quantum linear solver, in *AIAA AVIATION Forum and ASCEND 2025* (2025).

[14] Y. Cao, A. Papageorgiou, I. Petras, J. Traub, and S. Kais, Quantum algorithm and circuit design solving the Poisson equation, New Journal of Physics **15**, 013021 (2013).

[15] O. Koska, M. Baboulin, and A. Gazda, A tree-approach pauli decomposition algorithm with application to quantum computing (2024), arXiv:2403.11644 [quant-ph].

[16] J. R. McClean, S. Boixo, V. N. Smelyanskiy, R. Babbush, and H. Neven, Barren plateaus in quantum neural network training landscapes, Nature Communications **9**, 4812 (2018).

[17] A. Arrasmith, Z. Holmes, M. Cerezo, and P. J. Coles, Equivalence of quantum barren plateaus to cost concentration and narrow gorges, Quantum Science and Technology **7**, 045015 (2022).

[18] S. Aaronson, Read the fine print, Nature Physics **11**, 291 (2015).

[19] D. Camps, L. Lin, R. Van Beeumen, and C. Yang, Explicit quantum circuits for block encodings of certain sparse matrices, SIAM Journal on Matrix Analysis and Applications **45**, 801 (2024).

[20] C. Sünderhauf, E. Campbell, and J. Camps, Block-encoding structured matrices for data input in quantum computing, Quantum **8**, 1226 (2024).

[21] A. Boutot and V. Dsouza, Explicit block encodings of discrete Laplacians with mixed boundary conditions (2026), arXiv:2603.12405 [quant-ph].

[22] N. Hansen and A. Ostermeier, Completely derandomized self-adaptation in evolution strategies, Evolutionary Computation **9**, 159 (2001).

[23] N. Hansen, The CMA evolution strategy: A comparing review, in *Towards a New Evolutionary Computation*, Studies in Fuzziness and Soft Computing, Vol. 192, edited by J. A. Lozano, P. Larrañaga, I. Inza, and E. Bengoetxea (Springer, 2006) pp. 75–102.

[24] A. J. Chorin, Numerical solution of the Navier–Stokes equations, Mathematics of Computation **22**, 745 (1968).

[25] J. L. Guermond, P. Minev, and J. Shen, An overview of projection methods for incompressible flows, Computer Methods in Applied Mechanics and Engineering **195**, 6011 (2006).

[26] P. M. Gresho and R. L. Sani, On pressure boundary conditions for the incompressible Navier–Stokes equations, International Journal for Numerical Methods in Fluids **7**, 1111 (1987).

[27] M. Möttönen, J. J. Vartiainen, V. Bergholm, and M. M. Salomaa, Quantum circuits for general multiqubit gates, Physical Review Letters **93**, 10.1103/physrevlett.93.130502 (2004).

[28] A. Kandala, A. Mezzacapo, K. Temme, M. Takita, M. Brink, J. M. Chow, and J. M. Gambetta, Hardware-efficient variational quantum eigensolver for small molecules and quantum magnets, Nature **549**, 242 (2017).

[29] M. Cerezo, A. Sone, T. Volkoff, L. Cincio, and P. J. Coles, Cost function dependent barren plateaus in shallow parametrized quantum circuits, Nature Communications **12**, 1791 (2021).

[30] T. Hogancamp, R. Demirdjian, and D. Gunlycke, A linear combination of unitaries decomposition for the laplace operator (2026), arXiv:2601.06370 [quant-ph].

[31] T. Kharazi, A. M. Alkadri, J.-P. Liu, K. K. Mandadapu, and K. B. Whaley, Explicit block encodings of boundary value problems for many-body elliptic operators, Quantum **9**, 1764 (2025).